Product state resolved excitation spectroscopy of He–, Ne–, and Ar–Br_2 linear isomers: Experiment and theory

Jordan M. Pio, Wytze E. van der Veer, Craig R. Bieler,[a] and Kenneth C. Janda[b]
Department of Chemistry and Institute of Surface and Interface Science, University of California, Irvine, California 92697-2025, USA

(Received 22 January 2008; accepted 1 February 2008; published online 7 April 2008)

Valence excitation spectra for the linear isomers of He–, Ne–, and Ar–Br_2 are reported and compared to a two-dimensional simulation using the currently available potential energy surfaces. Excitation spectra from the ground electronic state to the region of the inner turning point of the Rg–Br_2 (B,ν') stretching coordinate are recorded while probing the asymptotic Br_2 (B,ν') state. Each spectrum is a broad continuum extending over hundreds of wavenumbers, becoming broader and more blueshifted as the rare gas atom is changed from He to Ne to Ar. In the case of Ne–Br_2, the threshold for producing the asymptotic product state reveals the X-state linear isomer bond energy to be 71 ± 3 cm^{-1}. The qualitative agreement between experiment and theory shows that the spectra can be correctly regarded as revealing the one-atom solvent shifts and also provides new insight into the one-atom cage effect on the halogen vibrational relaxation. The measured spectra provide data to test future *ab initio* potential energy surfaces in the interaction of rare gas atoms with the halogen valence excited state. © *2008 American Institute of Physics*. [DOI: 10.1063/1.2885047]

I. INTRODUCTION

The rare gas–halogen complexes have been studied extensively as model systems for a variety of dynamics, including vibrational and electronic predissociation and intramolecular vibrational energy redistribution.[1] Despite their apparent simplicity and 30 years of study, there have been many unresolved problems and controversies, including until recently, the details of the intermolecular potential energy surface.[2] Early microwave spectroscopy of Ar-ClF (Ref. 3) and Kr-ClF (Ref. 4) showed the structure of these complexes to be linear, with the rare gas atom attached to the chlorine, rather than a triangular structure expected for the assumed pairwise additive van der Waals interaction. Soon thereafter, the He–I_2 complex was first observed by Smalley *et al.*[5,6] via laser-induced fluorescence (LIF) of the halogen $X \rightarrow B$ electronic transition, and the spectrum was best fit assuming a T-shaped structure for the complex.[6] The $X \rightarrow B$ spectra for many other rare gas–halogen complexes obtained thereafter also indicated T-shaped structures (see Tables I and II of Ref. 2 and references therein). The major exception to the preponderance of data pointing to T-shaped structures was the observation that the excitation of Ar–I_2 above the I_2 B-state dissociation limit produces fluorescence from bound I_2 (B,ν').[7,8] It was proposed that this result was due to a one-atom cage effect in a linear Ar–I_2 complex.[8] Further experimental work[9–11] strengthened the case for the existence of the linear isomer of Ar–I_2.

Electronic structure calculations for the intermolecular potentials suggested the possibility of two rare gas–halogen isomers coexisting by predicting minima for both the linear and T-shaped configurations of the X-state intermolecular potential energy surface,[2,12–16] with the linear being at the global minimum. This surprisingly anisotropic potential was shown by Rohrbacher *et al.* to be in good agreement with spectroscopic and scattering data.[17] The *ab initio* predictions for the B state indicated an intermolecular potential much more consistent with a pairwise additive interaction.[13,18–21] While the T-shaped minimum in the B state changes only slightly compared to the X state, with a small increase in bond length and a small decrease in well depth, the linear minimum moves to a longer distance and becomes much shallower. The different anisotropies of the X- and B-state potentials result from the significant increase in electron density in the axial region of the halogen caused by the promotion of an electron to the σ^* orbital.[18,20] Theoretical studies of the $X \rightarrow B$ spectrum of the two isomers[22,23] explained that while the T-shaped isomer has strong discrete transitions from the significant overlap of the ground and excited state T-shaped minima, the linear isomer spectrum is dominated by a continuum due to the repulsive nature of the intermolecular potential in the B state at the X-state van der Waals bond length, as shown in Fig. 1. Recently, Loomis and coworkers have reported on the $X \rightarrow B$ spectra for a variety of linear rare gas–halogen complexes.[24–28] These spectra have both discrete features due to transitions to highly excited van der Waals bending modes as well as continua from excitation to the repulsive wall of the intermolecular potential. So far, though, no data have been reported that systematically compare the excitation spectra of a series of rare gas–halogen complexes as a function of the rare gas atom. In this paper we report on the $X \rightarrow B$ continuum spectra of the linear isomers of Rg–Br_2 (L-RgBr$_2$) for Rg=He, Ne, and Ar. The

[a]Present address: Department of Chemistry, Albion College, Albion, Michigan, USA.
[b]Electronic mail: kcjanda@uci.edu.

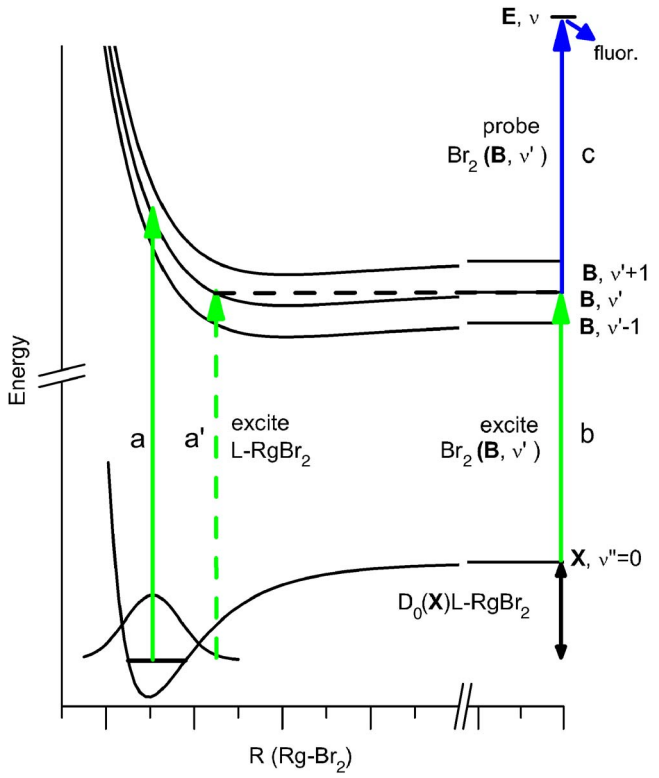

FIG. 1. (Color online) Diagram of pump-probe experiments and intermolecular potential energy surfaces for linear $Rg-Br_2$. The energies at large R are those of the free Br_2 (X,ν''), (B,ν'), and (E,ν) states. Free Br_2 double resonance excitation is represented by transition (b) followed by transition (c). Excitation of the L-$RgBr_2$ continuum is represented by transition (a). The threshold excitation for the onset of the continuum is represented by transition (a').

results presented here provide insight into how the intermolecular potential energy surface for the B state changes in going from He to Ar.

II. EXPERIMENT

The $X \rightarrow B$ spectra of the linear $Rg-Br_2$ isomers are studied by a method similar to that of Loomis and co-workers.[24–28] The $X \rightarrow B$ excitation to a single L-$RgBr_2$ (B,ν') intermolecular potential energy surface is recorded by fixing the probe laser to detect the product Br_2 (B,ν') while the pump laser is scanned. For convenience, we will refer to the state that is formed when the rare gas atom attaches to Br_2 in the (B,ν') state as $Rg-Br_2$ (B,ν'). Referring to Fig. 1, while transition (a) simultaneously excites L-$RgBr_2$ to multiple intermolecular potential energy surfaces, only the excitation to the Br_2 (B,ν') surface is recorded because the probe laser is set to transition (c). These excitation or "action" spectra can be used to obtain the ground state binding energy of the linear isomer by determining the lowest excitation energy, transition (a'), at which the continuum signal begins.[24]

The experimental apparatus is similar to that used in our recent T-shaped $Ne-Br_2$ and $Ar-Br_2$ works.[29,30] A rare gas mixture (100% He for $He-Br_2$ complexes, 20% Ne/80% He for $Ne-Br_2$ complexes or 1% Ar/99% He for $Ar-Br_2$ complexes) is passed over a natural isotopic mixture of Br_2 held at $-16\ ^\circ C$. The rare gas–Br_2 mixture undergoes supersonic free jet expansion through a 150 μm diameter pulsed nozzle into a vacuum chamber, causing rapid cooling and leading to the formation of van der Waals complexes. The complexes are then studied using pump-probe spectroscopy. The pump and probe laser pulses are generated from two optical parametric oscillator–optical parametric amplifiers pumped by a single mode-locked neodymium doped yttrium aluminium garnet laser.[31] The temporal and frequency resolutions of the pulses are about 15 ps and 2 cm^{-1}, respectively. The pulses pass collinearly into the vacuum chamber and intersect the free jet 15 mm downstream from the nozzle. As illustrated in Fig. 1, the pump laser excites the complexes from the X ground electronic state of Br_2 to the B state. The product Br_2 (B,ν') from the photodissociation of the van der Waals complex is excited by the probe laser to the E state, from which fluorescence is detected using a photomultiplier tube. Spectra where the pump laser is scanned over several hundred wavenumbers are normalized to the pump laser intensity using a photodiode.

Because the spectra of the linear isomers are spread out over hundreds of wavenumbers, the intensity at any given wavelength is very weak, so much effort was spent optimizing the signal detection. The primary source of noise in our experiments is scattering of the probe laser from the body of the nozzle and the entrance and exit ports of the vacuum chamber. The scattered light is minimized by a combination of spatial filtering of the probe laser, careful adjustment of the size of the openings in the ports, and coating the reflective valve body with colloidal graphite. With these measures taken, the scattered light intensity from the probe laser is nearly zero even with the photomultipler tube (an Electron Tube 9558QB) at a relatively high −1600 V with a gain of 10^7, giving our experimental apparatus excellent dynamic range.

III. RESULTS

A sample excitation spectrum for linear $Ne-Br_2$ (L-$NeBr_2$) is shown in Fig. 2 (note that Figs. 2 and 3 each have the intensity shown on a logarithmic scale). This excitation spectrum was obtained by scanning the pump laser to the blue side of the uncomplexed $^{79}Br_2$ $X \rightarrow B$, $0 \rightarrow 16$ transition, indicated by the dashed line, while probing the $^{79}Br_2$ $B \rightarrow E$, $16 \rightarrow 2$ transition. Once the excitation energy reaches the threshold value needed to form product $^{79}Br_2$ $(B,\nu'=16)$, in this case at 18 090 cm^{-1}, there is an abrupt rise in the signal relative to the background. The 72 cm^{-1} blueshift of this onset from the free $^{79}Br_2$ $X \rightarrow B$, $0 \rightarrow 16$ transition is represented in Fig. 1 by the energy of the continuum onset, transition (a'), minus the energy of the free Br_2, transition (b). This energy difference is exactly the ground state binding energy of the linear complex, $D_0(X)$. Analogous spectra were recorded using other probe transitions ($^{79}Br_2$ $14 \rightarrow 1$, $^{79,81}Br_2$ $14 \rightarrow 1$, $^{79,81}Br_2$ $17 \rightarrow 3$), and a similar blueshift for the continuum onset was measured in each case. From these results, we assign a value for the linear $Ne-Br_2$ ground state binding energy of $D_0(X,\text{L-NeBr}_2) = 71 \pm 3\ cm^{-1}$. The error bars are assigned from the width of the onset which is between 5 and 6 cm^{-1}. All the measured blueshifts using dif-

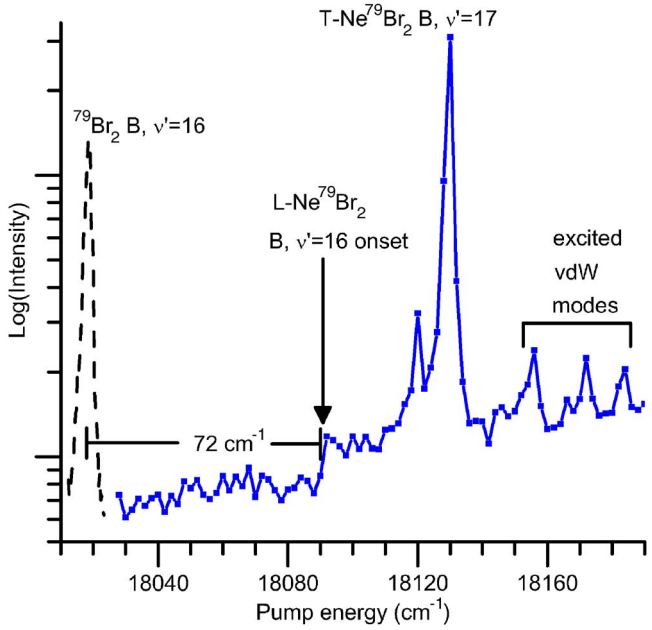

FIG. 2. (Color online) Excitation spectrum displaying the onset of the L-Ne^{79}Br$_2$ B, $\nu'=16$ continuum. The pump laser is scanned to the blue of the ^{79}Br$_2$ $X\rightarrow B$, $0\rightarrow 16$ transition, while the probe is fixed on the ^{79}Br$_2$ $B\rightarrow E$, $16\rightarrow 2$ transition. The dashed line indicates the ^{79}Br$_2$ $X\rightarrow B$, $0\rightarrow 16$ LIF spectrum. The intensity is on a log scale to emphasize the continuum signals.

ferent probe transitions fell within these error bars. To within experimental error, the linear isomer binding energy is equal to the T-shaped $NeBr_2$ ground state binding energy of 70.0 ± 1.1 cm^{-1}.[32] These results are in good agreement with *ab initio* calculations by Prosmiti *et al.*[16] that predict the linear and T-shaped X-state binding energies to be 68.0 and 67.3 cm^{-1}, respectively.

Figure 2 also shows several discrete features in addition to the continuum. The largest peak is due to the T-shaped Ne–^{79}Br$_2$ $X\rightarrow B$, $0\rightarrow 17$ excitation transition. Upon excitation, this complex undergoes vibrational predissociation and transfers one quanta of Br_2 vibrational energy to the van der Waals bond, dissociating the complex and leading to the formation of ^{79}Br$_2$ $(B,v'=16)$ detected by the probe laser.[33] Just to higher energy of the T-shaped feature are three much smaller peaks (again, note that the intensity scale is logarithmic) most likely due to excited van der Waals stretching modes in the Ne–^{79}Br$_2$ $(B,\nu'=17)$ intermolecular potential. This series of four peaks beginning with the T-Ne^{79}Br$_2$ $(B,\nu'=17)$ feature can be fitted to a vibrational progression with frequency $\omega_e=32.7$ cm^{-1} and anharmonicity $\omega_e\chi_e=3.75$ cm^{-1}. Reid *et al.* calculated the Ne–Cl_2 van der Waals mode wavefunctions and energies[34] and found the stretching mode levels were well described by the frequency $\omega_e=31.78$ cm^{-1} and anharmonicity $\omega_e\chi_e=3.21$ cm^{-1}. Considering $NeCl_2$ and $NeBr_2$ have similar reduced masses and bond energies [$D_0=55.40$ cm^{-1} for the potential used in Ref. 34, while the measured T-$NeBr_2$ $D_0(B)=61.2$ cm^{-1} (Ref. 32)], the nearly equal frequencies and anharmonicities support the assignment of these transitions to excited van der Waals stretching modes.

Excitation spectra of linear He–, Ne–, and Ar–Br_2 are

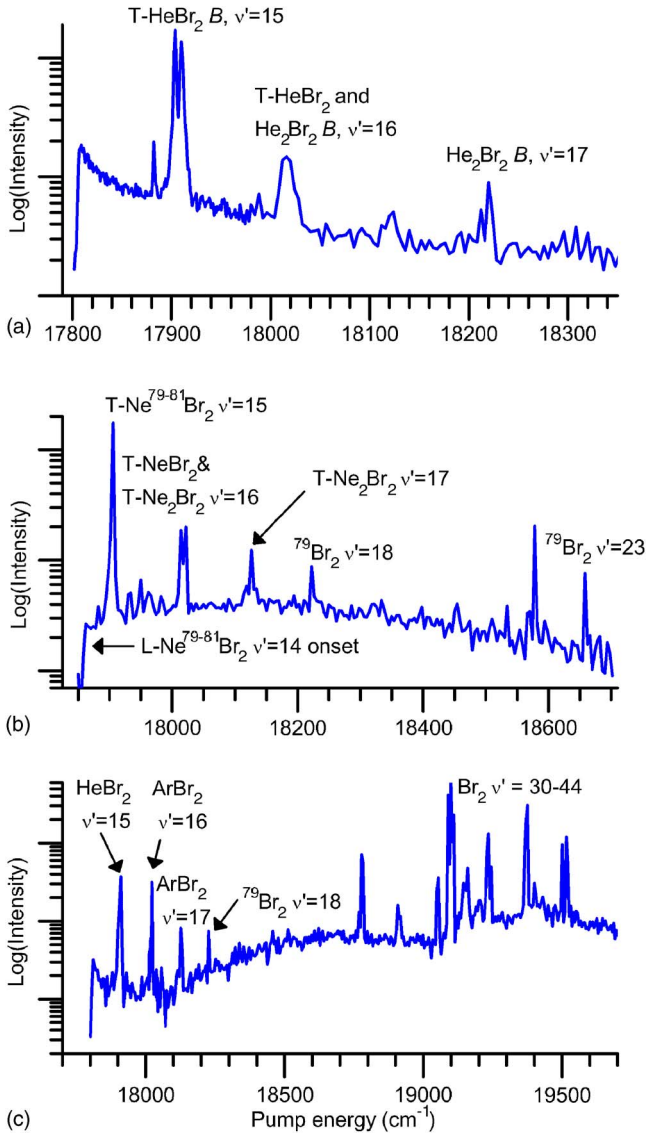

FIG. 3. (Color online) Excitation spectra of (a) L-He^{79,81}Br$_2$, (b) L-Ne^{79,81}Br$_2$, and (c) L-Ar^{79,81}Br$_2$ to the B, $\nu'=14$ intermolecular continuum. In each scan, the probe laser is fixed on the ^{79,81}Br$_2$ $B\rightarrow E$, $14\rightarrow 1$ transition. The intensity is on a log scale.

compared in Figs. 3(a)–3(c). For each of the spectra the probe laser was fixed on the ^{79,81}Br$_2$ $B\rightarrow E$, $14\rightarrow 1$ transition, and the pump laser was scanned to the blue side of the free ^{79,81}Br$_2$ $X\rightarrow B$, $0\rightarrow 14$ transition. This probe transition was chosen because it has minimal overlap with probe transitions originating from other (B,ν') levels. While there are still free Br_2 transitions in these spectra, especially at higher energies in the L-$ArBr_2$ spectrum, the intensities of these signals are very weak compared to the uncomplexed Br_2 $(B,\nu'=14)$ double resonance transition, so that contributions to the spectra from linear Rg–Br_2 (B,ν') other than $\nu'=14$ are negligible.

The spectrum of linear He–Br_2 in Fig. 3(a) begins with a very strong onset. In agreement with previous work on L-$HeBr_2$,[27] the position of the onset is blueshifted 17 cm^{-1} from the ^{79,81}Br$_2$ $X\rightarrow B$, $0\rightarrow 14$ transition. Immediately after the onset, the signal begins to decay, reaching its baseline value of 500 cm^{-1} above the onset.

When the He is replaced with Ne in the linear Rg–Br_2 complex, a much different continuum excitation spectrum is obtained. As with the linear Ne–Br_2 spectrum in Fig. 2, the L-$NeBr_2$ spectrum in Fig. 3(b) begins with a distinct continuum onset, with discrete T-shaped $NeBr_2$ features just to the blue of this onset, including the smaller peaks we assigned to excited van der Waals modes. Compared to the L-$HeBr_2$ spectrum, the onset is not nearly as strong. As the laser is scanned to the blue, the intensity of the continuum spectrum increases, peaking at around 18 150 cm^{-1} with about double the intensity of the onset. The spectrum for L-$NeBr_2$ also is broader than that of L-$HeBr_2$, spanning almost 800 cm^{-1}.

For the L-$ArBr_2$ spectrum, shown in Fig. 3(c), the onset is so weak that we cannot establish its position. So, we cannot determine the ground state linear bond energy. The intensity is clearly increasing at 18 100 cm^{-1}, which puts an upper limit of 311 cm^{-1} on the bond energy. The continuum increases in intensity for another 600 cm^{-1}, peaking at around 18 700 cm^{-1}. This result is similar to that for L-ArI_2 obtained by Darr *et al.*[26] A second, even more intense continuum starts at 19 000 cm^{-1}. That this second continuum is distinct from the first one was revealed by a source pressure dependence study. The intensity of the lower energy continuum is about as sensitive to the backing pressure of the gas mixture as the T-shaped Ar–Br_2 peaks, which is not surprising considering that the T-shaped and linear Ar–Br_2 isomers are expected to have similar ground state bond energies. This comparable pressure sensitivity of the T-shaped and linear isomers was also observed for He–Br_2 and Ne–Br_2 complexes. Because of the similarity to the L-ArI_2 spectrum and the pressure sensitivity of the intensity, we assign the lower energy continuum to the bound-free transitions of the L-$ArBr_2$ species, analogous to those of the other two linear species in Figs. 3(a) and 3(b).

In contrast, the higher energy continuum signal for L-$ArBr_2$ changes less with source pressure, so the relative intensities of the two continua depend on the pressure. For instance, with a 5 bar source pressure the intensity ratio between 18 700 and 19 300 cm^{-1} is $I(18\,700):I(19\,300)=0.24$. When the pressure is increased to 12 bars, the intensity ratio increases to $I(18\,700):I(19\,300)=0.64$. This is the opposite pressure dependence than would be expected if the second continuum was due to a higher cluster such as Ar_2Br_2.

Because it is not possible to spectroscopically size-select clusters with bound-free transitions of the linear isomers, the contribution to the continuum signals in the spectra of Fig. 3 from larger clusters must be reduced by adjusting the expansion conditions. This is especially critical for the Ne and Ar complexes that have a much greater tendency to cluster than does He. For the L-$NeBr_2$ spectrum in Fig. 3(b), the spectrum was taken at a gas pressure of 5 bars. At this pressure, there was no evidence of discrete transitions from clusters with more than two neon atoms. Because the discrete Ne_NBr_2 transitions are from clusters with the neons attached perpendicular to the Br–Br axis,[35] and discrete transitions due to Ne_2Br_2 are clearly present in Fig. 3, it is conceivable that a linear Ne–Br–Br–Ne complex is also present and contributing to the continuum. However, we expect the perpendicular Ne_2Br_2 to be the dominant di-Ne species since the favorable Ne–Ne interactions will give it a lower energy than Ne–Br–Br–Ne. Therefore, the broad continuum signal of Fig. 3(b) is due mainly to bound-free transitions of the linear Ne–Br_2 isomer. To test the effects of larger clusters on the continuum signal, the same excitation scan was taken using a higher pressure of 15 bars. Discrete transitions due to Ne_3Br_2 and Ne_4Br_2 complexes were observed. The continuum spectrum obtained at this higher pressure peaked at the same excitation energy as the low pressure scan.

For the L-$HeBr_2$ spectrum, the backing pressure for the scan was 12 bars, a relatively low pressure for studying He–Br_2 complexes. (Other studies[27,36] typically used pressures between 20 and 30 bars.) Since no discrete features due to clusters larger than He_2Br_2 are observed and T-shaped He–Br_2 signals are much greater than the He_2Br_2 peaks, it is unlikely that the continuum spectrum shown in Fig. 3(a) has significant contributions from larger clusters.

Similarly, the L-$ArBr_2$ spectrum was taken at backing pressures of 5, 12, and 17.5 bars; the 12 bar scan is shown in in Fig. 3(c). The intensity of the background continuum up to 19 000 cm^{-1} increased with increasing pressure. However, there was no change in the structure of the spectrum, indicating that even at the higher backing pressures larger clusters are not contributing significantly to the spectrum. As mentioned above, the intensity of the continuum signal above 19 000 cm^{-1} was not pressure sensitive.

IV. TWO-DIMENSIONAL MODEL SPECTRA

The continuum spectra reported here for the three linear Rg–Br_2 complexes demonstrate the sensitivity of the spectra to the intermolecular potential energy surfaces. We have simulated these spectra using a two-dimensional model.[37] In this model, the Rg–Br_2 complex is held fixed in a collinear orientation. The complex is described by the coordinates r, the Br–Br distance, and R, the distance between the rare gas atom and the Br_2 center of mass. The total spectrum is calculated as a product of Br_2 r-coordinate Franck–Condon factors (FCFs) and the R-coordinate spectrum obtained by using the reflection principle for the ground state van der Waals wavefunction onto the repulsive wall of the B-state intermolecular potentials.

The Rg–Br_2 X state is treated as two uncoupled oscillators, and the ground state Hamiltonian $\hat{H}_X$ is separable in the two coordinates,

$$\hat{H}_X = -\frac{\hbar^2}{2\mu_{Br_2}}\frac{\partial^2}{\partial r^2} + V_{X,Br_2}(r) - \frac{\hbar^2}{2\mu_{vdW}}\frac{\partial^2}{\partial R^2} + V_{X,vdW}(R)$$
$$= \hat{H}_{X,Br_2} + \hat{H}_{X,vdW}, \quad (1)$$

where the van der Waals coordinate reduced mass $\mu_{vdW} = m_{Rg}m_{Br_2}/m_{Rg}+m_{Br_2}$. Under the separability assumption the total wavefunction is a product of the Br–Br and Rg–Br_2 wavefunctions,

$$\Psi_{X,\nu'',n''}(r,R) = \chi_{X,\nu''}(r)\phi_{X,n''}(R). \quad (2)$$

The quantum numbers ν'' and n'' indicate the degree of vibrational excitation in the r and R coordinates, respectively.

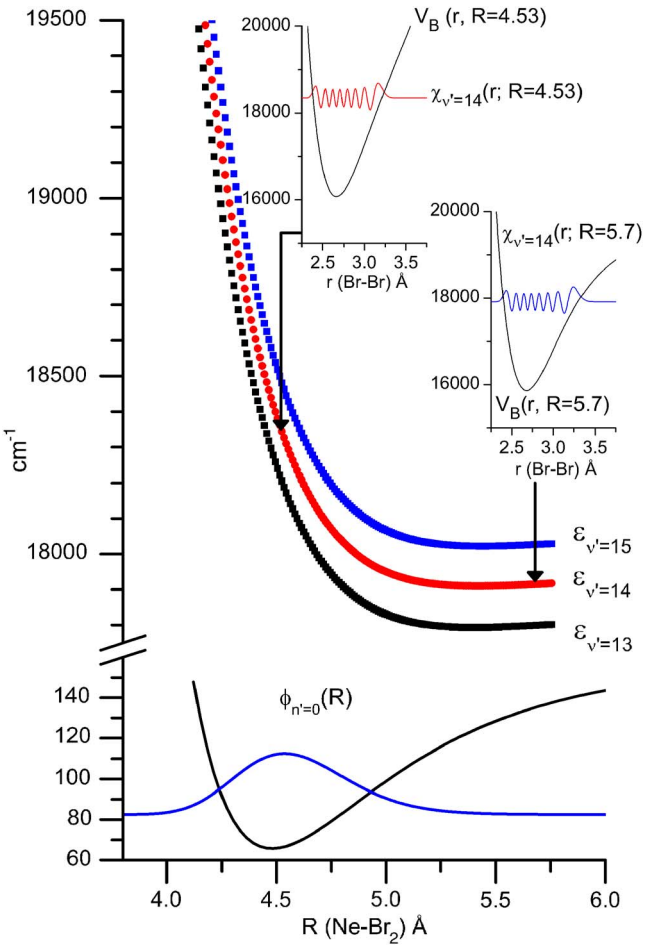

FIG. 4. (Color online) The lower portion of the figure shows the L-$NeBr_2$ ground state van der Waals potential energy surface and wavefunction. In the upper portion are the L-$NeBr_2$ B-state intermolecular potential energy surfaces $\epsilon_{\nu'}(R)$ for $\nu'=13-15$ calculated using the adiabatic approximation. Shown in the insets are the Br_2 potential energy surfaces $V_B(r;R=4.53$ Å) and $V_B(r;R=5.70$ Å), and the wavefunctions $\chi_{B,\nu'=14}(r;R=4.53$ Å) and $\chi_{B,\nu'=14}(r;R=5.70$ Å) obtained when the Schrodinger equation is solved using the Hamiltonian in Eq. (4).

The wavefunctions $\chi_{X,\nu''}(r)$ and $\phi_{X,n''}(R)$ and energies $\epsilon_{X,\nu'',n''}$ are obtained by solving the one-dimensional Schrodinger equations for r and R numerically using a discrete variable representation (DVR).[38] Grid sizes 0.0075 and 0.005 Å are used for the r and R coordinates. The Rydberg–Klein–Rees (RKR) potential of Ref. 39 is used for the Br–Br potential $V_{X,Br_2}(r)$, and the *ab initio* potentials of Ref. 16 are used for the Rg–Br_2 potential $V_{X,vdW}(R)$. As an example, the van der Waals wavefunction calculated numerically for L-$NeBr_2$ in its ground vibrational level and the *ab initio* potential are plotted in the lower half of Fig. 4. Because the van der Waals bending motions with their inherent zero point energy are not considered in the one-dimensional potential, the energy of the van der Waals mode is lower than that calculated using the three-dimensional intermolecular potential. The one-dimensional D_0 values calculated here for linear He–, Ne–, and Ar–Br_2 are 26, 78, and 244 cm^{-1}, compared to 17.2, 68.0, and 228.0 cm^{-1} when the bending motions are included.[16]

Because excitation to the B state goes to the repulsive region of the van der Waals coordinate, the presence of the rare gas atom highly perturbs the Br–Br interaction, so that this interaction is no longer well approximated by the free Br–Br potential. Thus, the excited state Hamiltonian cannot be separated,

$$\hat{H}_B = -\frac{\hbar^2}{2\mu_{Br_2}}\frac{\partial^2}{\partial r^2} - \frac{\hbar^2}{2\mu_{vdW}}\frac{\partial^2}{\partial R^2} + V_B(r,R). \quad (3)$$

Assuming that the vibrational eigenenergies and wavefunctions of Br_2 vary smoothly with the rare gas distance R, Eq. (3) can be approximated by assuming an adiabatic separation between the coordinates.[37] In this approximation, the van der Waals coordinate is treated as a parameter, so that Eq. (3) becomes an effective one-dimensional function of r, with R being fixed,

$$\hat{H}_{B,Br_2}(r;R) = -\frac{\hbar^2}{2\mu_{Br_2}}\frac{d^2}{dr^2} + V_B(r;R). \quad (4)$$

Solving the Schrodinger equation for this one-dimensional Hamiltonian, the resulting Br–Br vibrational wavefunctions $\chi_{B,\nu'}(r;R)$ and energies $\epsilon_{\nu'}(R)$ have a parametric dependence on the van der Waals coordinate. The variation of the Br_2 vibrational energies $\epsilon_{\nu'}$ with R form the R-dependent intermolecular potential energy surfaces for each Br_2 B-state vibrational energy level ν'.

These curves are calculated by solving Eq. (4) for a range of R values chosen to coincide with the range of the X-state van der Waals wavefunction in its ground vibrational state, $\phi_{X,n''=0}(R)$. Beginning with the minimum R value, the wavefunctions $\chi_{B,\nu'}(r;R)$ and energies $\epsilon_{\nu'}(R)$ are calculated using the same DVR method and r-coordinate grid size as for the X state. R is then incremented by 0.01 Å, and Eq. (4) is solved again. This procedure is repeated until the desired range for R is obtained.

The critical input to this computational procedure is the two-dimensional potential energy surface, $V_B(r,R)$. As the experimental results show, changes in the potential energy surface lead to very different spectra, which make this work well suited for testing *ab initio* results for van der Waals interactions both in the ground and excited electronic states. Only for He–Br_2 have *ab initio* results for the B-state potential been reported.[20] However, theoretical studies on the vibrational predissociation dynamics of T-shaped He–,[40] Ne–,[32,41] and Ar–Br_2 (Ref. 30) have been able to reproduce the experimental results using a simple atom-atom pairwise additive potential, with a Morse potential for the Rg–Br interaction and the B-state RKR potential of Ref. 39 for the Br–Br interaction. We used the same form of the potential for these calculations, as well as the same Morse potential parameters D_e, α, and R_e, which are recorded in Table I. While

TABLE I. Morse potential parameters used for Rg–Br interaction in the pairwise additive B-state potential.

Rg	D_e (cm^{-1})	α_e (Å^{-1})	R_e (Å)
He	17	1.55	3.92
Ne	42	1.67	3.90
Ar	114	1.80	4.10

the potential parameters in these studies were chosen to reproduce the T-shaped dynamics, using the same potential parameters for the calculations in the linear configuration should give at least qualitatively accurate results because, as noted above, the B-state intermolecular interaction is not highly anisotropic. The two-dimensional B-state potential energy surface in terms of r and R is

$$V_B(r,R) = V_{B,\mathrm{Br}_2}(r) + D_e(1 - e^{-\alpha(R-(r/2)-R_e)})^2 + D_e(1 - e^{-\alpha(R+(r/2)-R_e)})^2 - 2D_e. \quad (5)$$

The RKR Br–Br potential was extended to short-r with the 12-parameter Br_2 B-state potential of Tellinghuisen.[42,43] This addition to the potential is necessary because the Br_2 bound states will have their inner turning points at these short-r distances when the rare gas atom is close.

The upper half of Fig. 4 displays the resulting intermolecular potential energy surfaces $\epsilon_{\nu'}(R)$ of these adiabatic calculations for L-$NeBr_2$, $\nu'=13$, 14, and 15. Each vertical series of energies at a fixed value of R are the Br_2 vibrational eigenenergies obtained from numerically solving Eq. (4). Shown in the insets are the corresponding Br_2 $(B,\ \nu'=14)$ wavefunctions $\chi_{B,\nu'=14}(r;R)$ and Br_2 potential energy curves $V_B(r;R)$ for $R=4.53$ and 5.7 Å. At large Ne distances the Br–Br interaction, vibrational energies, and wavefunctions approach their free Br_2 (B,ν') values. As the Ne distance decreases, the repulsion between the Ne and Br_2 increases, "pushing in" the outer branch of the Br_2 potential. This compression of the potential increases the energy of the vibrational levels and the energy spacing between the vibrational levels as well. This is shown in Fig. 4, with the energies and the vertical spacing between the $\epsilon_{\nu'}$ curves increasing with decreasing R. The effects on the wavefunctions are important to consider as well because the Br_2 Franck–Condon factors are highly dependent on the rare gas distance.

Once the L-$RgBr_2$ intermolecular potential energies and R-dependent Br_2 B-state wavefunctions are obtained, the two-dimensional excitation spectrum to a particular B, ν' intermolecular potential energy surface is calculated. Because the excitation in the van der Waals coordinate leads to fast, direct dissociation, the classical reflection principle can be applied to calculate the spectrum.[37,44] Under the reflection principle, the spectrum is a mapping of the ground state R-coordinate probability density onto the energy axis. The excitation energy E corresponding to the R-coordinate value R' is given by the difference between the ground and excited state potential energy surfaces: $\epsilon_{\nu'}(R') - V_{X,\mathrm{vdW}}(R') = E$. The intensity of the spectrum at E is proportional to the probability density of the ground state van der Waals wavefunction at R', $|\phi_{X,n''=0}(R')|^2$, and inversely proportional to the magnitude of the excited state potential's slope, $|\partial\epsilon_{\nu'}(R)/\partial R|^{-1}_{R=R'}$. The latter factor is necessary to account for the fact that steeper potentials spread the probabilty density over a wider range of energies, so that the intensity at any given energy becomes less. For the r-coordinate, the Br_2 Franck–Condon factor when $R=R'$ is calculated, and the total spectrum is then a product of the reflection principle spectrum of the van der Waals coordinate and the Br_2 FCF,

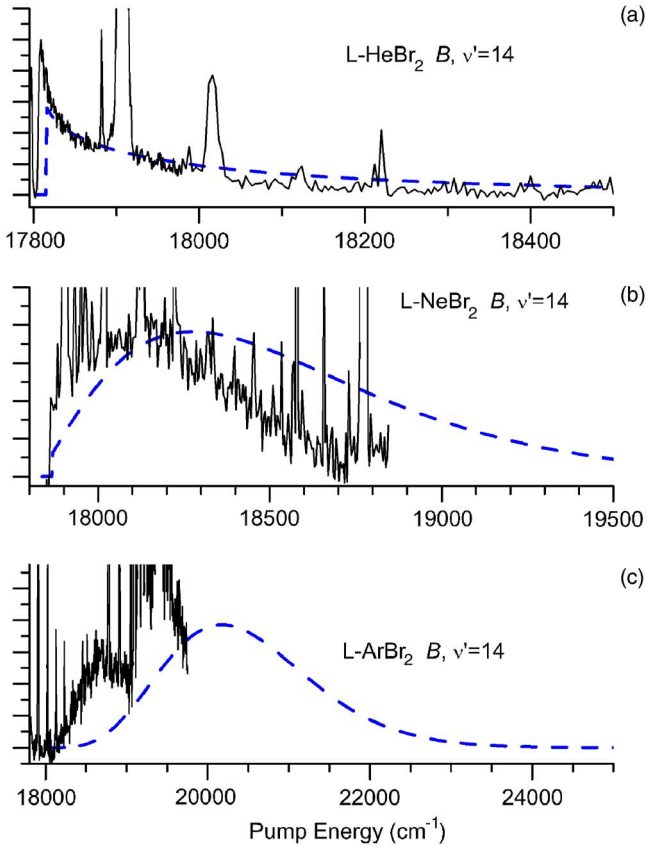

FIG. 5. (Color online) Calculated excitation spectra (dashed line) $\sigma_{\nu'}(E)$ of (a) L-$He^{79,81}Br_2$ (b) L-$Ne^{79,81}Br_2$ and (c) L-$Ar^{79,81}Br_2$ to the $(B,\nu'=14)$ adiabatic potential energy surfaces using Eq. (6). The experimental spectra (solid line) are reproduced from Fig. 3. The intensity is on a linear scale.

$$\sigma_{\nu'}(E) \propto E|\langle\chi_{B,\nu'}(r;R')|\chi_{X,\nu''=0}(r)\rangle|^2|\phi_X(R')|^2\left|\frac{\partial\epsilon_{\nu'}(R)}{\partial R}\right|^{-1}_{R=R'}. \quad (6)$$

If the excitation is not above the energy of the $\epsilon_{\nu'}$ asymptotic limit, i.e., $E<\epsilon_{\nu'}(R\to\infty)-\epsilon_{X,\nu''=0,n''=0}$, the intensity of the spectrum is set to zero.

Figure 5 shows the spectra for linear He–, Ne–, and Ar–Br_2 for $\nu'=14$ calculated using this two-dimensional adiabatic model. The experimental spectra from Fig. 3 are reproduced for comparison (note that here the intensity scale is linear, not logarithmic). The model spectra qualitatively reproduce the trends of the experimental spectra. The L-$HeBr_2$ spectrum peaks at the onset, while the L-$NeBr_2$ and L-$ArBr_2$ spectra peak further to the blue and are broader. Clearly, there are major differences between the calculated and experimental spectra, especially for L-$ArBr_2$, with the calculated spectra being broader and more blueshifted than the experimental spectra.

Because the ground state L-$HeBr_2$ has vertical transitions to the relatively flat portion of the intermolecular potential near the threshold energy, the classical reflection principle may not be as accurate for this portion of the spectrum. We recalculated the spectrum of the van der Waals coordinate by solving for the van der Waals continuum wavefunctions of the adiabatic B-state $\nu'=14$ intermolecular potential energy surface using the discrete variable representation. The

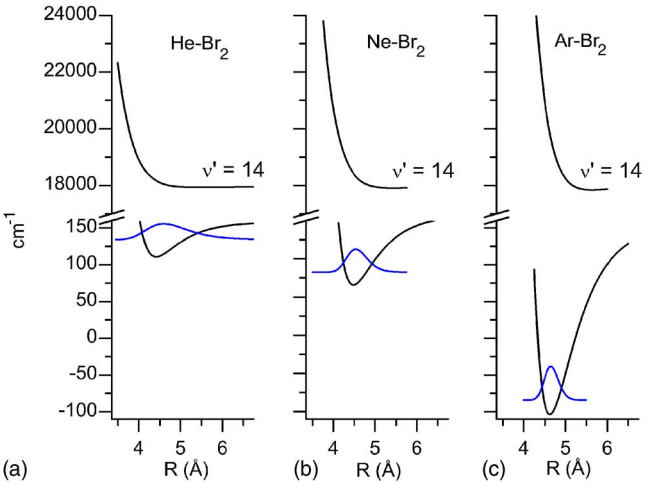

FIG. 6. (Color online) Calculated ground state van der Waals wavefunctions and excited state $(B, \nu'=14)$ adiabatic potential energy surfaces for (a) L-$He^{79,81}Br_2$, (b) L-$Ne^{79,81}Br_2$, and (c) L-$Ar^{79,81}Br_2$.

R-coordinate grid extended well into asymptotic region, with the last gridpoint being $R_{max}=50$ Å. The continuum wavefunctions obtained were energy normalized,[44] and the Franck–Condon factors per unit energy calculated to obtain the *R*-coordinate spectrum. For transition energies greater than 18 000 cm^{-1}, the one-dimensional reflection principle spectrum and the "exact" one-dimensional quantum mechanical spectrum for L-$HeBr_2$ are identical. Near the onset, the quantum mechanical spectrum has about twice the intensity as the reflection principle spectrum. The quantum mechanical spectra for linear Ne– and Ar–Br_2 were calculated as well, and the differences between these and the reflection principle spectra are negligible.

V. DISCUSSION

The bound-free spectra for linear He–, Ne–, and Ar–Br_2 presented here are continuum signals that extend over hundreds of wavenumbers, much like the L-ArI_2 excitation spectrum.[26] These broad continuum signals are the signature of the linear isomers of rare gas–halogens in the $X \rightarrow B$ spectral region.[9]

Even though all three rare gas–linear isomers give broad continuum spectra, the shapes of the spectra are quite sensitive to the identity of the rare gas atom, becoming wider and peaking at higher energies as the rare gas atom is changed from He to Ne to Ar. Using the calculations from the two-dimensional adiabatic model, the features of the spectra can be explained by examining the changes in van der Waals coordinate wavefunctions and potentials. Figures 6(a)–6(c) show the van der Waals *X*-state wavefunctions, potential energy surfaces, and the adiabatic *B*-state $\nu'=14$ intermolecular potential energy surfaces for all three L-$RgBr_2$ complexes. First consider L-$HeBr_2$, whose excitation spectrum to *B*, $\nu'=14$ [Fig. 3(a)], has an intense signal at the threshold energy but begins to decrease immediately to the blue. In Fig. 6(a), the ground state van der Waals wavefunction is highly delocalized because of the light He atom and the shallow well of the intermolecular potential. Thus, the wavefunction has significant intensity at the larger-*R* distances corresponding to transitions at the threshold energy, leading to the observed intense onset. Another cause for the strong onset is the minimal repulsive interaction between the He atom and the Br_2 $(B, \nu'=14)$ at *R*-values corresponding to the peak region of the ground state wavefunction. Consequently, vertical transitions near the onset energy will have contributions near the peak region of the van der Waals wavefunction. Since only the short-*R* tail of the wavefunction has transitions to the repulsive wall of the *B*, $\nu'=14$ intermolecular potential, the continuum signal decreases immediately after the onset, reflecting the decrease in the ground state wavefunction's amplitude with decreasing *R*.

In contrast to L-$HeBr_2$, the excitation spectrum of L-$ArBr_2$ peaks at much higher energy and has negligible intensity at threshold. As shown in Fig. 6(c) the intermolecular potential energy surface in the *X* state has a deeper well due to the greater polarizability of the Ar atom. This, along with the larger Ar mass, results in a much more localized Ar–Br_2 stretching wavefunction in the *X* state. Because the wavefunction is very localized, it does not have significant amplitude at the large-*R* values corresponding to the threshold excitation energy [as is the case for transition (a') in Fig. 1], leading to the weak intensity at threshold. In the excited state, the intermolecular potential energy at *R* values corresponding to the peak region of the ground state wavefunction is highly repulsive from the greater overlap of electron density between the Br_2 and the Ar atom. Because the entire wavefunction is projected onto the steep, repulsive region of the excited state adiabatic intermolecular potential, the resulting spectrum is much broader than that of L-$HeBr_2$. Both the more attractive ground state interaction and the more repulsive excited state interaction combine to give the much larger blueshift for L-$ArBr_2$ compared to L-$HeBr_2$. It is interesting to note that a similar interpretation was offered by Kerenskaya *et al.*[45] for the origin of the blueshifts of the Br_2 visible spectrum in various condensed phase environments. With this in mind, the blueshifts observed in the L-$RgBr_2$ spectra could be viewed as "one-atom solvent shifts."

The results for both the calculated and experimental L-$NeBr_2$ spectra are consistent with the above discussion. Since the Ne atom's mass, size, and polarizability are in between those of He and Ar, the L-$NeBr_2$ spectrum's onset intensity, width, and blueshift are intermediate those of the L-$HeBr_2$ and L-$ArBr_2$ spectra.

The preceding discussion focused on the role of the van der Waals coordinate in determining the spectrum. However, in the adiabatic model the effect of the Br–Br coordinate is not negligible. As discussed below, the Br_2 adiabatic vibrational wavefunctions $\chi_{B,\nu'}(r;R)$ mix in free Br_2 *B*-state vibrational wavefunctions from higher vibrational levels that have better overlap with the Br_2 ground state wavefunction. Thus, the Br_2 FCFs change dramatically as the rare gas atom distance changes. Using the excitation of L-$NeBr_2$ $(B, \nu'=14)$ as an example, at large Ne distances, the Br_2 FCFs are calculated here to be 5.6×10^{-4}. In contrast, the Br_2 $(B, \nu'=14)$ wavefunction when the Ne atom is at 4.53 Å (shown in the inset of Fig. 4) has much better overlap with the Br_2 $(X, \nu''=0)$ wavefunction, and the FCFs increase significantly to 2.7×10^{-3}. Since the Br_2 $(X, \nu''=0)$ wavefunction peaks at

2.28 Å, the better overlap is from the Br_2 $(B, \nu'=14)$ wavefunction having greater amplitude at the short-r distances as the Br–Br potential is compressed by the Ne atom, as can be seen by comparing the two Br_2 wavefunctions in the insets of Fig. 4. The increasing FCFs with decreasing R partially offset the decrease in the L-$NeBr_2$ wavefunction at R values shorter than 4.54 Å, leading to an even broader, more blue-shifted spectrum than would be obtained by just applying the one-dimensional reflection principle to the R-coordinate.

While the two-dimensional adiabatic model is successful at explaining the general trends in the L-$RgBr_2$ spectra, discrepancies between the experimental and the calculated spectra are significant. There are two major sources of error in our calculated spectra. The first is the adiabatic assumption of the model. The kinetic energy of the van der Waals coordinate can couple the states from different B, ν' intermolecular potentials, and this coupling increases on the repulsive portion of the adiabatic intermolecular potential. The second source of error is from the inaccuracies in the assumed potential energy surfaces, and better agreement could be achieved with adjustments to the Rg–Br Morse potential parameters. The discrepancies are particularly large for the L-$ArBr_2$ spectra because, as discussed above, almost all of the van der Waals wavefunction is reflected onto the repulsive wall of the excited state adiabatic intermolecular potential. So, the spectrum is much more sensitive to the details of the potential and to errors from the adiabatic approximation. That all three calculated spectra in Fig. 5 are overly broad indicates that the repulsive portions of the intermolecular potentials are too steep. While more exact close coupling or wavepacket calculations should be used to rigorously test any assumed intermolecular potentials, the two-dimensional adiabatic model has the advantage of giving a relatively simple and intuitive picture for interpreting the results.

Since we have successfully modeled the wide excitation spectra of the L-$RgBr_2$ species as transitions to repulsive walls of the intermolecular continua, the results appear to support the conclusion of Darr *et al.*[26] that the continuum fluorescence of L-ArI_2 first attributed to one-atom caging is largely due to direct excitation of the van der Waals bond, with very little one-atom caging. However, it must be noted that Franck–Condon excitation of the halogen coordinate also goes to the highly repulsive portion of the halogen B-state potential. For example, the projection of the $Ar-Br_2$ ground state wavefunction $\Psi_{X,\nu''=0,n''=0}(r,R)$ onto the $V_B(r,R)$ potential creates a wavepacket that is mainly localized on the repulsive wall of the Br–Br B-state potential, while the potential for the initial wavepacket is only mildly repulsive in the R coordinate. Classically, the swarm of trajectories would accelerate primarily in the r-direction before colliding with the $Ar-Br_2$ repulsive wall, leading to substantial kinetic energy transfer to the R coordinate. This effect will be even more pronounced as the excitation is shifted to higher energy: Franck–Condon excitations corresponding to these energies go to even more strongly repulsive portions of the r coordinate. This picture is consistent with wavepacket calculations on linear $Ar-I_2$ that show that one-atom caging is significant at excitation energies near the I_2 dissociation limit.[46]

Whether the dynamics of the linear Rg–X–X isomer photodissociation for energies above the X–X dissociation limit is referred to as a "one-atom cage effect" or not depends on the precise definition of the "cage effect." In the limit of solution phase chemistry, caging usually refers to geminate recombination: The chromophore dissociates to form two radicals and then reforms because the solvent keeps the fragments close enough together so that they eventually recombine. That certainly is not the case for the linear Rg–X–X isomer. Instead, we see that the excess photon energy is initially divided between the $Rg-X_2$ R coordinate and the X–X r coordinate. For high enough photon energies, enough energy is deposited into the r coordinate so that, in the absence of the rare gas atom, the halogen would dissociate. However, as the wavepacket evolves after excitation, the excess energy is almost immediately transferred to the weak bond of the dissociative R coordinate. So, in this more restricted sense there can be said to be a cage effect as opposed to a direct excitation of the dissociative coordinate. Thus, our current understanding of the cage effect is quite similar to that described by Fang and Martens.[46] The details of the dynamics may be slightly different from that described by Fang and Martens in that the ground state Rg–X bond length for the linear isomer is now known to be shorter than they assumed, so the energy transfer from the halogen stretch to the dissociative coordinate occurs earlier in the dissociative trajectory than they calculated. Instead of dissociation recombination, perhaps the process should be described as inhibited dissociation.

It is interesting to consider how the adiabatic model incorporates the insight from the wavepacket perspective. Although the adiabatic potential correlates to a single free Br_2 (B,ν') stretching state at large R, more and more free Br_2 (B,ν') stretching wavefunctions contribute to the adiabatic Br_2 wavefunction as the the R coordinate becomes more repulsive. That is, when the adiabatic wavefunction $\chi_{B,\nu'}(r;R)$ is expanded in the basis of free Br_2 (B,ν') stretching states, the contributions from stretching levels above the asymptotic product level increase with increasing repulsion in the R coordinate. So, the expectation value for the kinetic energy in the r coordinate is also quite high when R is in the repulsive region because of the contributions from higher Br_2 stretching excited states. As an example, for $Ar-Br_2$ $(B,\nu'=14)$ the calculated Br–Br kinetic energy expectation value $\langle\chi_{B,\nu'=14}(r;R)|\hat{T}_{Br_2}|\chi_{B,\nu'=14}(r;R)\rangle$ is 1360 cm^{-1} when the Ar atom is at its ground state equilibrium distance of $R=4.65$ Å. After the Ar atom has dissociated, the free Br_2 $(B,\nu'=14)$ has a mean kinetic energy of 826 cm^{-1}, corresponding to a kinetic energy transfer of 534 cm^{-1}. Thus, while the explanation of the continuum signals as excitation to the intermolecular continuum is consistent with the experimental results and calculations presented here, this explanation does not exclude the possibility of the substantial transfer of kinetic energy from the halogen to the van der Waals coordinate. Perhaps the best answer to the question of how much of the dynamics should be attributed to caging could be obtained by evaluating the halogen kinetic energy as a function of time in a full six-dimensional wavepacket analysis.

Although we have been focusing on the continuum portion of the spectra, there are also many discrete features. The assignments of some of these features are given in Fig. 3. Some others remain unidentified. This is partly due to the fact that the probe transition has weak overlap with other transitions and even very weak discrete transitions can have intensities comparable to the continuum. The L-$NeBr_2$ spectra contain a series of discrete transitions which we suggest are due to excited van der Waals stretching modes. That these transitions could be fitted to a vibrational progression with a frequency and anharmonicity in good agreement with a theoretical study for $NeCl_2$ gives support to this assignment. Obtaining lifetime data and product state distributions of these transitions would be quite useful in making a firmer identification. If these transitions are due to excited van der Waals modes, it will be particularly interesting to see how the lifetime of the T-shaped complex depends on amount of excitation in the van der Waals coordinate. As discussed for $NeCl_2$, the dependence of the lifetime on the van der Waals vibrational level is not obvious.[47]

Another interesting feature is the second continuum at high energies in the L-$ArBr_2$ spectrum. While the total intensity at energies greater than 19 000 cm^{-1} remained the same upon increasing the source pressure from 5 to 12 bars, the relative contribution to the intensity from the unknown high energy continuum decreased with increasing pressure, since the contribution of the lower energy continuum to the intensity increased. We speculate that the unknown continuum may be due to excitation originating from the first excited van der Waals stretching mode in the ground state, and the high energy continuum is a reflection of the short-R portion of the wavefunction. Thus, as the pressure is increased, yielding a cooler distribution of initial states, the second continuum becomes less intense relative to the first one. That there is no evidence of the long-R portion of the excited van der Waals stretching wavefunction at lower energy may be because it is reflected onto the portion of the excited state intermolecular potential below the threshold energy. While the L-$HeBr_2$ ground state potential is too shallow to support an excited stretching mode, this is not the case for L-$NeBr_2$, so that scanning L-$NeBr_2$ spectra even further to the blue than was done for the spectrum in Fig. 3(b) may reveal a similar high energy continuum. We note that a second continuum was seen in the L-ArI_2 continuum spectrum,[26] but this continuum was well separated from the low energy continuum. It is clear that the spectra of these molecules still contain considerable information to be revealed in future studies.

VI. SUMMARY AND CONCLUSIONS

The data reported here on the $X \rightarrow B$ continuum spectra for linear isomers of Rg–Br_2 represent the first systematic comparison of the spectra of linear rare gas–halogen complexes for a series of rare gas atoms. While the spectra for linear He–, Ne–, and Ar–Br_2 are all broad continuum signals, the features of the continuum signals depend strongly on the Rg–Br_2 interaction. The spectra become much broader and more blueshifted as the rare gas atom is changed from He to Ne to Ar. The trends in the spectra are reproduced and explained using a simple two-dimensional model that assumes that the excited state potential energy curves are vibrationally adiabatic with regard to the bromine stretch. From the L-$NeBr_2$ spectra, the L-$NeBr_2$ ground state bond energy was found to be 71 ± 3 cm^{-1}, equal to that of the T-shaped isomer within experimental error.

That the simple two-dimensional adiabatic model provided here gives qualitative agreement with the measured spectra strongly suggests that the physics of dissociation is best described as direct excitation to the van der Waals continuum. However, this does not exclude the possibility of one-atom caging, and the adiabatic model indicates that a significant amount of kinetic energy is transferred from the halogen to the van der Waals coordinate after the excitation is complete. Further theoretical analysis will be required to determine whether errors in the potential or an incomplete model are the most important sources of quantitative disagreement. Clearly *ab initio* results for the repulsive region of the B-state potential would be very valuable for a more detailed analysis. Also, it would not be surprising if electronic nonadiabaticity makes a contribution to the dynamics. For a more complete analysis it would also be useful to acquire excitation spectra to higher product vibrational levels.

In these broad spectra, multiple features are observed that have yet to be identified. The L-$ArBr_2$ spectrum contains a second continuum at high excitation energies that we speculate may be due to transitions from the excited van der Waals stretching mode in the ground state. In the $NeBr_2$ spectrum there is a series of discrete transitions that we tentatively assign to excited $NeBr_2$ van der Waals modes. Future work on the time resolved dynamics and product state distributions of these levels may provide an excellent opportunity to explore how the dynamics of the complex changes with increasing excitation in the van der Waals degree of freedom.

The noble gas–halogen complexes continue to be a fascinating model system for testing our insight and theories for both potential energy surfaces and the molecular dynamics that occur on those surfaces. Originally, those of us working on these problems thought that they would provide simple models for understanding more complex systems. After many years of study, we now understand that these model systems are not so simple after all. Much of the confusion about these species was cleared up once it was realized that the stabilities of the linear and T-shaped isomers are about equal in the ground electronic state. The T-shaped isomers have been much more intensively studied, and so the potential energy surfaces of the excited states in the vicinity of T-shaped geometry are reasonably well characterized. So far, little effort has been devoted to obtaining accurate potentials for excited states in the linear geometry. Data such as reported here can be used for that purpose. Unlike data for the T-shaped isomer, the linear isomer data offer considerable information regarding the repulsive portion of the potential. Although a preliminary analysis of the data has been performed here, extraction of reliable potential surface information will require the use of a more accurate dynamics model.

In the near future, we hope to extend the present study to H_2O-halogen dimers for which the blueshifts of the excitation spectra should be even more dramatic.

As *ab initio* results become available for the intermolecular interactions of these complexes, especially in the electronically excited *B* state, the experimental results presented could prove to be an excellent test for the reliability of the electronic structure calculations. We look forward to the day when *ab initio* calculations and experiment are in complete agreement.

ACKNOWLEDGMENTS

We gratefully acknowledge R. A. Loomis for communicating to us his observations of linear $Ne-Br_2$ and for encouraging the study reported here. We thank N. Halberstadt, O. Roncero, and V. A. Apkarian for the helpful discussions and comments. This work has been supported by the U.S. National Science Foundation, Award Nos. CHE-0213149 and CHE-0404743.

[1] A. Rohrbacher, N. Halberstadt, and K. C. Janda, Annu. Rev. Phys. Chem. **51**, 405 (2000).
[2] A. Rohrbacher, J. Williams, and K. C. Janda, Phys. Chem. Chem. Phys. **1**, 5263 (1999).
[3] S. J. Harris, S. E. Novick, W. Klemperer, and W. E. Falconer, J. Chem. Phys. **61**, 193 (1974).
[4] S. E. Novick, S. J. Harris, K. C. Janda, and W. Klemperer, Can. J. Phys. **53**, 2007 (1975).
[5] R. E. Smalley, D. H. Levy, and L. Wharton, J. Chem. Phys. **64**, 3266 (1976).
[6] R. E. Smalley, L. Wharton, and D. H. Levy, J. Chem. Phys. **68**, 671 (1978).
[7] K. L. Saenger, G. M. McClelland, and D. R. Herschbach, J. Phys. Chem. **85**, 3333 (1981).
[8] J. J. Valentini and J. B. Cross, J. Chem. Phys. **77**, 572 (1982).
[9] M. L. Burke and W. Klemperer, J. Chem. Phys. **98**, 1797 (1993).
[10] A. Burroughs, T. V. Marter, and M. C. Heaven, J. Chem. Phys. **111**, 2478 (1999).
[11] M. C. Cockett, D. A. Beattie, R. J. Donovan, and K. P. Lawley, Chem. Phys. Lett. **259**, 554 (1996).
[12] F.-M. Tao and W. Klemperer, J. Chem. Phys. **97**, 440 (1992).
[13] G. Chalasinski, M. Gutowski, M. M. Szczesniak, J. Sadlej, and S. Scheiner, J. Chem. Phys. **101**, 6800 (1994).
[14] J. Sadlej, G. Chalasinski, and M. M. Szczesniak, J. Mol. Struct.: THEOCHEM **307**, 187 (1994).
[15] S. S. Huang, C. R. Bieler, K. C. Janda, F.-M. Tao, W. Klemperer, P. Casavecchia, G. G. Volpi, and N. Halberstadt, J. Chem. Phys. **102**, 8846 (1995).
[16] R. Prosmiti, C. Cunha, P. Villarreal, and G. Delgado-Barrio, J. Chem. Phys. **116**, 9249 (2002).
[17] A. Rohrbacher, K. Janda, L. Beneventi, P. Casavecchia, and G. Volpi, J. Phys. Chem. A **101**, 6528 (1997).
[18] S. M. Cybulski, R. Burcl, G. Chalasinski, and M. M. Szczesniak, J. Chem. Phys. **103**, 10116 (1995).
[19] A. Rohrbacher, J. Williams, K. C. Janda, S. M. Cybulski, R. Burcl, M. M. Szczesniak, G. Chalasinski, and N. Halberstadt, J. Chem. Phys. **106**, 2685 (1997).
[20] M. P. de Lara-Castells, A. A. Buchachenko, G. Delgado-Barrio, and P. Villarreal, J. Chem. Phys. **120**, 2182 (2004).
[21] A. Valdes, R. Prosmiti, P. Villarreal, G. Delgado-Barrio, and H.-J. Werner, J. Chem. Phys. **126**, 204301 (2007).
[22] K. C. Janda, D. Djahandideh, O. Roncero, and N. Halberstadt, Chem. Phys. **239**, 177 (1998).
[23] O. Roncero, B. Lepetit, J. A. Beswick, N. Halberstadt, and A. A. Buchachenko, J. Chem. Phys. **115**, 6961 (2001).
[24] J. P. Darr, A. C. Crowther, and R. A. Loomis, Chem. Phys. Lett. **378**, 359 (2003).
[25] S. E. Ray, A. B. McCoy, J. J. Glennon, J. P. Darr, E. J. Fesser, J. R. Lancaster, and R. A. Loomis, J. Chem. Phys. **125**, 164314 (2006).
[26] J. P. Darr, J. J. Glennon, and R. A. Loomis, J. Chem. Phys. **122**, 131101 (2005).
[27] D. S. Boucher, D. B. Strasfeld, R. A. Loomis, J. M. Herbert, S. E. Ray, and A. B. McCoy, J. Chem. Phys. **123**, 104312 (2005).
[28] J. P. D. David, B. Strasfeld, and R. A. Loomis, Chem. Phys. Lett. **397**, 116 (2004).
[29] J. A. Cabrera, C. R. Bieler, B. C. Olbricht, W. E. van der Veer, and K. C. Janda, J. Chem. Phys. **123**, 054311 (2005).
[30] J. Cabrera, C. R. Bieler, N. McKinney, W. E. van der Veer, J. M. Pio, K. Janda, and O. Roncero, J. Chem. Phys. **127**, 164309 (2007).
[31] W. E. van der Veer, Laser Focus World **37**, 141 (2001).
[32] M. Nejad-Sattari and T. A. Stephenson, J. Chem. Phys. **106**, 5454 (1997).
[33] N. Sivakumar, J. Cline, C. R. Bieler, and K. C. Janda, Chem. Phys. Lett. **147**, 561 (1988).
[34] B. P. Reid, K. C. Janda, and N. Halberstadt, J. Phys. Chem. **92**, 587 (1988).
[35] B. A. Swartz, D. E. Brinza, C. M. Western, and K. C. Janda, J. Phys. Chem. **88**, 6272 (1984).
[36] D. G. Jahn, W. S. Barney, J. Cabalo, S. G. Clement, A. Rohrbacher, T. J. Slotterback, J. Williams, K. C. Janda, and N. Halberstadt, J. Chem. Phys. **104**, 3501 (1996).
[37] R. Schinke, *Photodissociation Dynamics: Spectroscopy and Fragmentation of Small Polyatomic Molecules* (Cambridge University Press, Cambridge, 1993), Chaps. 2, 3, and 6, pp. 38–41, 61–67, and 109–112.
[38] D. T. Colbert and W. H. Miller, J. Chem. Phys. **96**, 1982 (1992).
[39] R. Barrow, T. Clark, J. Coxon, and K. Yee, J. Mol. Spectrosc. **51**, 428 (1974).
[40] A. Rohrbacher, T. Ruchti, K. C. Janda, A. A. Buchachenko, M. I. Hernández, T. González-Lezana, P. Villarreal, and G. Delgado-Barrio, J. Chem. Phys. **110**, 256 (1999).
[41] T. A. Stephenson and N. Halberstadt, J. Chem. Phys. **112**, 2265 (2000).
[42] J. Tellinghuisen, J. Chem. Phys. **115**, 10417 (2001).
[43] J. Tellinghuisen, J. Chem. Phys. **118**, 1573 (2003).
[44] J. Tellinghuisen, Adv. Chem. Phys. **60**, 299 (1985).
[45] G. Kerenskaya, I. Goldschleger, V. Apkarian, and K. Janda, J. Phys. Chem. A **110**, 13792 (2006).
[46] J.-Y. Fang and C. C. Martens, J. Chem. Phys. **105**, 9072 (1996).
[47] N. Halberstadt, O. Roncero, and J. A. Beswick, Chem. Phys. **129**, 83 (1989).